Minimizing Polymer Curl Distortion and Heat Impact to Improve DLP Printing Accuracy via Subdivision Method

Sirawit Pruksawan[a], Yi Ting Chong[a], Yang Zhao[a], Vinod Kumar S/O Sivaraja[a], Andrew Chun Yong Ngo[a], Peng Jin[a,b], FuKe Wang[a,*]

[a] *Institute of Materials Research and Engineering (IMRE), Agency for Science, Technology and Research (A*STAR), 2 Fusionopolis Way, Innovis #08-03, Singapore 138634, Republic of Singapore*

[b]State Key Laboratory of Coking Coal Resources Green Exploitation, China Pingmei Shenma Group, Pingdingshan 467000, People's Republic of China

***Corresponding author: FK Wang**

Institute of Materials Research and Engineering (IMRE)

Agency for Science, Technology and Research (A*STAR)

2 Fusionopolis Way, Innovis #08-03

Singapore 138634

Email: wangf@imre.a-star.edu.sg

Abstract

Curl distortion has been a persistent challenge for vat photopolymerization (VPP)-based printing technology such as Digital Light Processing (DLP), leading to structural deformation and print failures. This study presents a new approach to mitigate curling distortion and heat effects during DLP printing by dividing the printing layer image into sequential sub-images, using a breadth-first search (BFS) algorithm. The progressive curing process, resembling a ripple pattern, results in a significant improvement in printing accuracy. The deviation was reduced tenfold when the layer image was divided into sub-images with 10 pixels for a 32 mm diameter disc. Additionally, subdivision strategy helps to reduce the heat effect during photopolymerization, as monitored *in situ* by a long-wave infrared (LWIR) camera. The successful reduction of residual stress using the subdivision strategy resulted in a 75% improvement in the mechanical performance of the printed products. We also demonstrate that the simple adoption of subdivision strategy in practical 3D printing applications. For solid 3D printing structures, introducing intervals within the solid printing layers—such as using a grid structure instead of a fully solid one, can help to reduce curling and heat effects, thereby improving 3D printing accuracy.

Keywords

Curl distortion, volume shrinkage, vat photopolymerization, DLP, printing accuracy, heat effect, acrylates

1. Introduction

Additive manufacturing, mostly referred to as 3D printing, has become a valuable technology for producing complex and high-precision structures with minimal material waste and ease of production [1]. The process begins with a 3D model created in computer-aided design (CAD) software, which is then converted into a Standard Tessellation Language (STL) or Additive Manufacturing File (AMF) to control the layer-by-layer 3D printing process. The affordability of 3D printing methods has made it a practical manufacturing technology in various industries, including aerospace, automotive, biomedicine, construction, arts, and jewellery [2]. In particular, 3D printing has become increasingly important in biomedical engineering applications due to its ability to quickly customize products [3].

Vat photopolymerization (VPP) based 3D printing technologies, including laser scanning-based stereolithography (SLA) and UV light projection-based methods like digital light processing (DLP), are among the most widely used 3D printing methods due to their fast printing speed, high resolution, and smooth surface finishes[4]. VPP based 3D printing builds structures layer by layer through the photopolymerization of resins. Acrylates, the most used photo-curable resins, often suffer from high shrinkage stress during curing, leading to internal stress and dimensional inaccuracies[5]. In SLA, where polymerization occurs point by point, shrinkage is localized and gradual, minimizing internal stress and reducing distortion[6]. In contrast, DLP cures an entire layer simultaneously, causing uniform shrinkage across the entire layer. This rapid and layer-wide shrinkage generates significant internal stress, resulting in polymer warping and dimensional inaccuracies. Polymer shrinkage significantly hinders the accuracy of DLP printing, especially in biomedical and engineering applications where precision is critical, despite DLP's advantage in high printing speed. Furthermore, the entire layer photopolymerization process during DLP printing generates heat through an exothermic reaction, causing the temperature to rise rapidly. This results in both volume

expansion due to the exothermic reaction and shrinkage after thermal exchange surrounding resins. This dynamic process creates non-uniform internal stress, leading to further structure inaccuracies and curl distortion during the printing process [7]. The accumulated residual stress also brings adverse effect on the mechanical performance of the printed parts. As a result, challenges of resin shrinkage and heat-induced deformation represent major obstacles for current applications of DLP printing technology.

Various strategies have been developed to reduce the shrinkage caused by photopolymerization from different perspectives. One approach involves modifying materials, such as incorporating inorganic fillers or replacing (meth)acrylates with cyclic monomers like cyclic ketene acetals, spiro orthoesters, or vinylcyclopropanes[8], This approach requires significant time and extensive experimental work to find the ideal formula and often request the specifically customized 3D printing conditions for each formula. Another approach is to minimize shrinkage by optimizing the printing files. This is typically achieved through a compensation method, where polynomial regression models analyze shrinkage in the *x*, *y*, and *z*-axis directions[9]. By employing these models, CAD files are modified to compensate for shrinkage. However, this approach is dependent on product geometry and may not be applicable to all manufacturing processes. Recently, significant efforts have been made to improve the DLP 3D printing dimensional accuracy by using grayscale technique[10]. In this method, the grayscale of each pixel is optimized for each layer's printing file to compensate for distortions. However, optimizing the grayscale often requires programming optimization or machine learning. While this method shows specific advantage in surface smoothing, it frequently encounters issues of over-curing or under-curing.

In the present study, we investigate both the heat effect and polymer shrinkage induced curling during the DLP 3D printing process and propose a subdivision strategy to mitigate the

curling issue. We divided individual projection image into sub-images and curing them in a ripple development pattern from the centre to the edge. The result shows a significant decrease in structural deviation, and the subdivision strategy effectively reduces the heat effect during photopolymerization. As a further development and application of this strategy in practice, we found that designing a grid structure, rather than a solid structure, can remarkedly improve printing accuracy. This approach is straightforward and does not require additional printer modifications or sophisticated computer programming. It offers a practical solution to enhance printing accuracy for most DLP printing tasks, potentially expanding the practical applications of DLP 3D printing technology in high-accuracy demanding fields such as healthcare and engineering.

2. Results and Discussion

2.1 Strategy for Reducing Shrinkage-Induced Curling of Polymers

Acrylates and (Meth)acrylates are extensively utilized in current vat photopolymerization-based 3D Printing techniques, however, the issue of high shrinkage stress associated with these resins remains a major challenge for their widespread applications in 3D-printing technologies [5a, 7b]. The phenomenon of photo-polymerization-induced shrinkage stress occurs during the phase transition from a liquid to a solid state. During the liquid state, monomers interact with each other through van der Waals forces with a distance of approximately 3.4 Å. During polymerization, these monomers are then covalently bonded with a reduced distance of 1.5 Å, resulting in volumetric shrinkage of the acrylates and leading to stress, which is primarily manifested as curl and creep distortions in the resulting solid structures [11]. In the present study, 1,6-Hexanedioldiacrylate (HDDA) (Figure S1), a typical acrylate with high volumetric shrinkage (*VS*), was selected. The

volumetric shrinkage of HDDA was measured in percentage from density of the monomer (D_m) and polymer (D_p) of HDDA according to equation (1):

$$VS = \frac{(D_p - D_m)}{D_p} \times 100\% \qquad (1)$$

Density of HDDA before and after photopolymerization were measured according to Archimedes' principle with a commercial density determination kit of the analytical balance for at least three times. Based on the density change measurement, volumetric shrinkage of HDDA was calculated to be 13.5 ± 0.67 % according to equation (1), indicating a significant shrinkage ratio of HDDA after photopolymerization.

As HDDA resin is transparent, light penetration through the printing layer into the previously formed layers, leads to over-curing and uneven solidification. To eliminate this over-curing induced distortion effect, the HDDA-based resin was mixed with carbon black or pigments to absorb and shield light. The content of the photoinitiator and carbon black was optimized based on previously reported curing depth studies [12].

Figure S2 illustrates a printed disc structure based on its CAD file by using HDDA as printing ink. The high volumetric shrinkage of HDDA makes even a simple disc structure challenging to print on a DLP printer due to remarkable polymer-shrinkage induced delamination. During the printing process in DLP, curl distortions occur as the top layer shrinks after bonding to the previous layers. The curl stress is dependent on both the degree of shrinkage of the printing layer and the interlayer shear stresses generated during the layer-by-layer printing process. The accumulated curling leads to substantial structural distortions in the final printed product and affect its printing accuracy and mechanical properties. Moreover, the curing-induced structural deformation weakens the attachment of subsequent layers to the previous layer, resulting in delamination of the printed layer and detachment of the printed object from the printing platform, causing printing failure (Figure S3). Therefore, controlling the shrinkage of each individual layer during the object building process in DLP

printing will reduce curl stress in each layer, as well as the accumulated curl distortion of the entire structure.

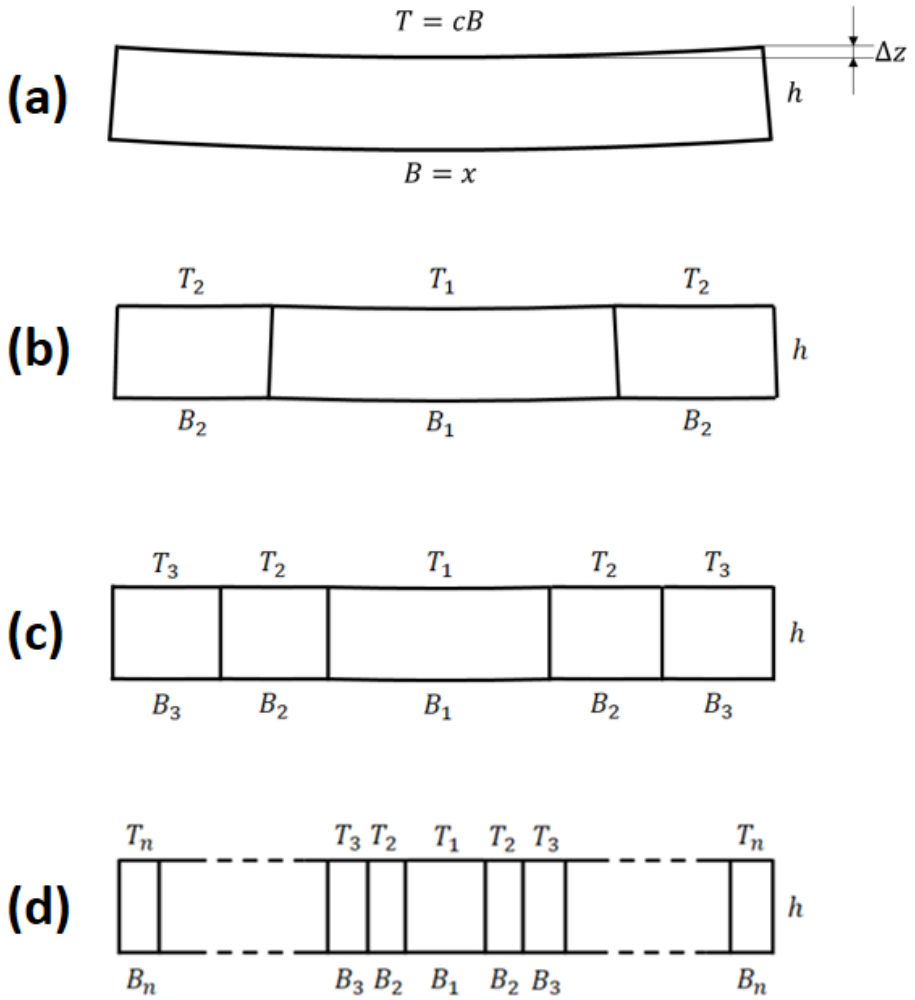

Figure 1 Illustration of the subdivision strategy. Pattern with (a) n = 1 (b) n = 2 (c) n = 3 (d) n = $\propto$ and the predicted shrinkage profile.

To address this problem, we propose the use of a subdivision strategy to eliminate the shrinkage-induced distortion as shown in Figure 1. The idea behind this strategy is to reduce shrinkage by subdividing each layer into smaller, concentric rings. Subdivision has been successfully used in the past to improve the resolution of 3D models by adding more polygonal faces to the STL file [13]. In our approach, the width of the top surface is represented by *T*, and the width of the bottom surface is represented by *B*. Under normal

curing conditions using a DLP printer, the entire layer is exposed to light at once. This can lead to significant curling up in materials with high shrinkage. We assume that the top surface shrinks evenly and the width of the top surface is given by $T = cB$, where c is the shrinkage constant that represents the intrinsic property of the material. To simplify our calculations and evaluations, we use the profile of a circular layer. The maximum displacement in the vertical direction, Δz, can be calculated using the following equation:

$$\Delta z = r - r\,cos\left(\frac{T}{2r}\right) \qquad (2)$$

Where r is the radius of the top curled surface as defined in Figure 2. The shrinkage in the thickness, h, is ignored for individual layers due to its small value (most printers have a layer thickness of between 25 and 50 μm). According to equation (2), it is evident that the maximum displacement (Δz_{max}) is positively correlated with the width of the top face (T). In other words, reducing the width of the curing width (value of T) will result in a decrease in the amount of distortion (value of Δz_{max}).

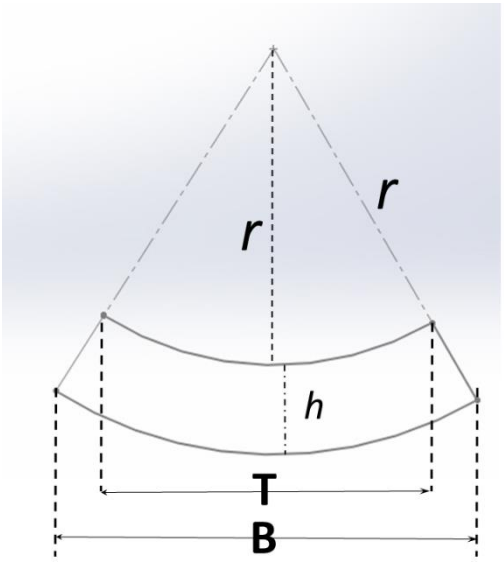

Figure 2 The definition of curled radius in equation (2).

To achieve this, we propose the progressive curing approach in the present work. The progressive curing approach involves solidifying each individual layer from the center to the

periphery, similar to the ripple development process. As shown in Figure 3 for the comparison of the subdivision strategy, the central part of the layer is solidified first, followed by the next circular ring. This process is repeated until the entire layer is solidified. By implementing the subdivision strategy and the progressive curing approach, we aim to decrease the width of the curing surface and, as a result, minimize the amount of distortion in the final printed product.

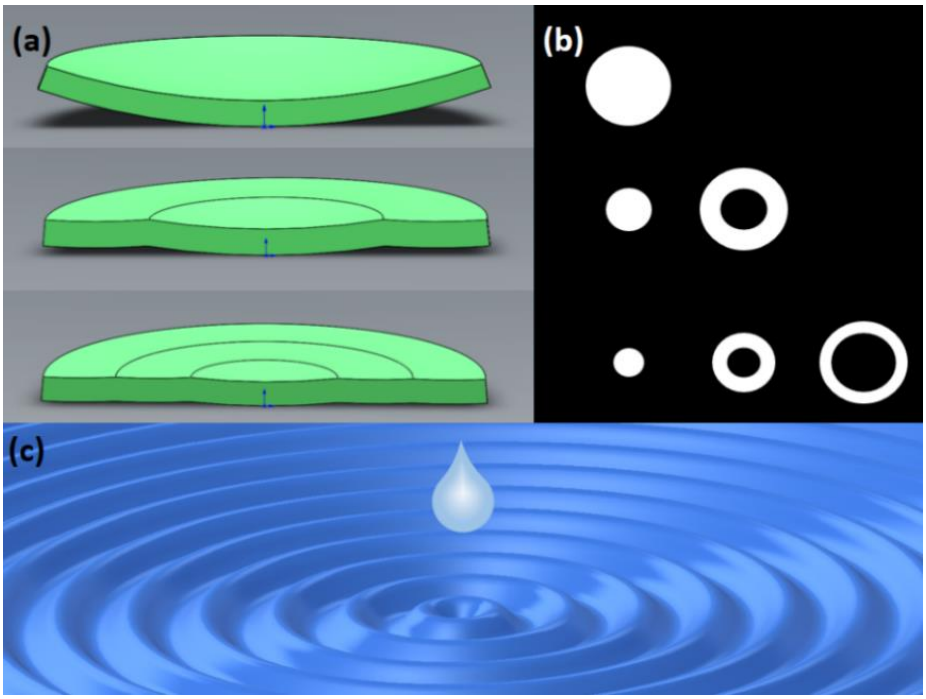

Figure 3 Illustration of the integration of subdivision strategy with ripple development-like curing process. (a) Curling distortion with different number of segmentations curing for each individual layer. (b) The employing of subdivision strategy to divide each cross-section image into different number of segmentations. The top diagram shows the normal strategy in current DLP printing process, with entire image projected at once. The center and bottom diagram show the light exposure for same size layer with 2 and 3 segments respectively. (c) Ripple development on water surface, which is similar to the light curing process from center to the edge in the present work.

The profile can then be described with the following equations:

$$B_k = \begin{cases} \frac{1}{n}x & (k = 1) \\ \frac{1}{2n}x & (k > 1) \end{cases} \quad (3)$$

$$T_k = \begin{cases} \frac{1}{n}cx & (k = 1) \\ c(\Delta_{k-1} + B_k) & (k > 1) \end{cases} \quad (4)$$

$$\Delta_k = \begin{cases} \frac{1}{n}(1-c)x & (k = 1) \\ (1-c)(\Delta_{k-1} + B_k) & (k > 1) \end{cases} \quad (5)$$

where n is the total part count for exposure, and Δk is the length difference between the top and bottom line in the kth division.

To evaluate the deformation, the maximum displacement of each exposure, Δz_k, is calculated using the following equation:

$$\Delta z_k = \begin{cases} r - r\,cos\left(\frac{T_k}{2r}\right) & (k = 1) \\ r - r\,cos\left(\frac{T_k}{r}\right) & (k > 1) \end{cases} \quad (6)$$

The overall maximum displacement (Δz_{max}) is calculated as the maximum value of Δz_k of each exposure. From the previous equations, it can be seen that Δz_{max} decreases with the increase in n, indicating that a finer segmentation of the cross-section image will result in less distortion. This is because when the inner part is exposed to light, polymer shrinkage will draw liquid resin towards the center region to compensate for shrinkage. This flow of resin during each exposure reduces internal stress and increases with the number of exposures. The compensation effect continues until the total shrinkage deformation approaches zero as the number of exposures approaches infinity. In contrast, if curing starts from the outer regions and progresses toward the center (opposite to the direction of ripple development), the outer segment will cure first, forming a seal around the uncured center. When the center eventually cures, the shrinkage will not be compensated by the surrounding resin flow, leading to the formation of gaps. This results in poor mechanical performance and reduced printing accuracy.

2.2. Subdivision Strategy for Reducing Heat Effect

The subdivision strategy is also effective in reducing the heat effect during the polymerization process. As it well known that a significant amount of heat is generated during free radical photopolymerization because of the splitting of the carbon double bond and formation of new bonds, and the Trommsdorff effect[14]. Exothermic photopolymerization leads to temperature rise and resin swelling due to thermal expansion. After the auto-acceleration process, the temperature decreases, leading to resin shrinkage caused by thermal contraction. This results in accumulation of the residue stress, which lead to the delamination and reduced mechanical performance. However, employing subdivision strategy helps to reduce amount of heat generation during photopolymerization, and the ripple curing process from center to the edge assists heat release to the environment.

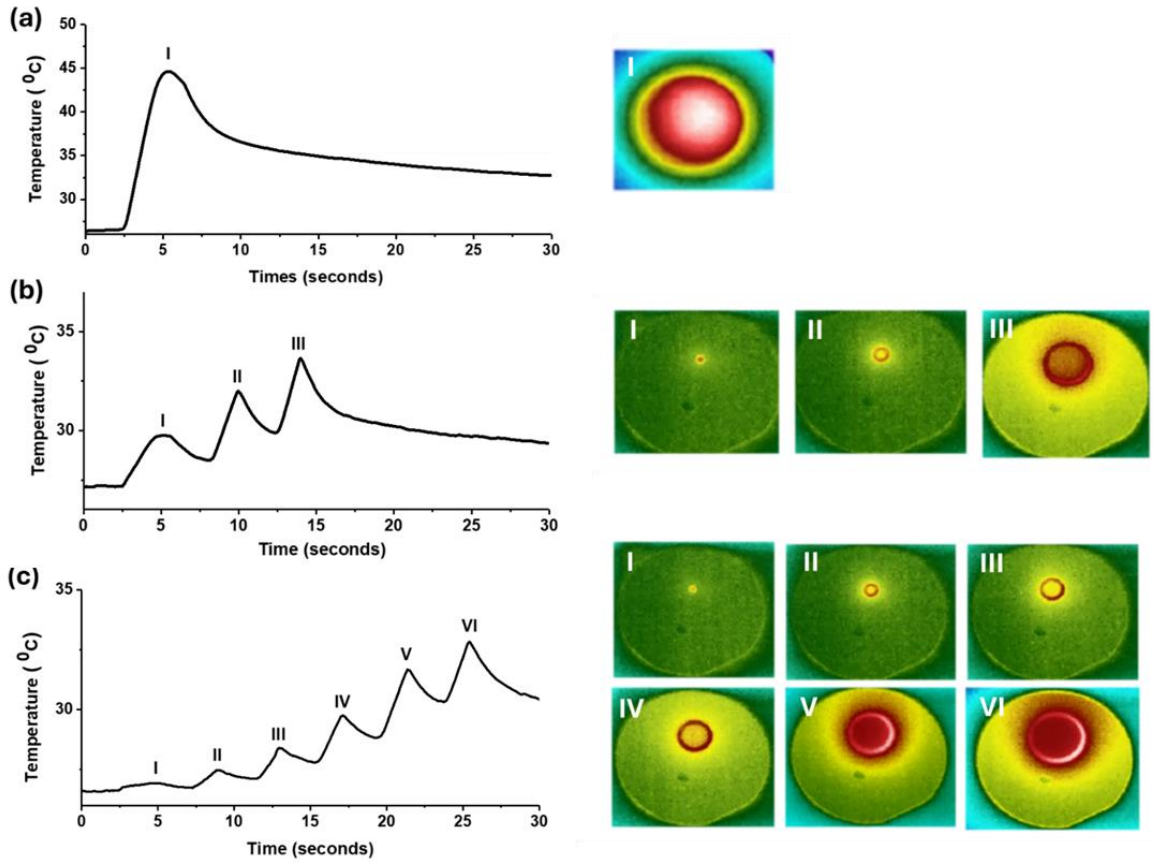

Figure 4 Temperature evolution of the resin cured by different projection modes. (a) The disc (Diameter: 20 mm; Thickness: 0.1 mm) is built by projecting the whole disc to the resin as normal. (b) The same disc is built by dividing it into 3 sub-images and cured from

center to the edge using the ripple manner. (c) The same disc is built by dividing it into 6 sub-images and cured from center to the edge using the ripple manner.

To investigate the effectiveness of the subdivision strategy in reducing the heat effect during the 3D printing process, we monitored the temperature of the resin using a long-wave infrared (LWIR) camera. A video was recorded to visually demonstrate the variation in the resin temperature during the curing process under three different curing modes. Figure 4a shows the experimental setup and Figure 4b-d display the temperature evolution of the resin during the curing process under different curing modes. Corresponding infrared images of the resin are also inserted above the temperature curve for better understanding.

Obviously, without employing the subdivision strategy, the resin temperature significantly increased to 44.6 ℃ after 4 seconds of light exposure when a disc with diameter of 20 mm and thickness of 0.1 mm was projected onto the resin with a 4-second light exposure due to the Trommsdorff effect (Figure 4b). However, when the subdivision strategy was employed, a significant decrease in temperature was observed. For example, when the same disc was divided into 3 sub-images as shown in Figure 4c, and the extracted images were exposed to light continually one by one from center to the edge. The highest resin temperature was only 33.6 °C. Further subdivision of the same image led to a continuing decrease in temperature and less temperature changes. In Figure 4d, the same sized disc was projected with 6 concentric circles (rings), resulting in the highest temperature of 32.8 ℃ only. This was because less heat was generated as less resin was cured each time when the subdivision strategy was used, and the sequential curing from center to the edge facilitated heat release to the environment. These results demonstrate that the integration of the subdivision strategy and ripple curing process can effectively reduce curl distortion by decreasing the heat effect during the 3D printing process.

2.3 Enhancing Printing Accuracy by Employing Subdivision Strategy

To illustrate the effect of subdivision effect on the printing accuracy and mechanical performance, a simple disc structure was chosen as a model to demonstrate how the subdivision strategy can reduce the curing distortion. This structure was selected for its ease of printing and evaluation. The diameter of the structure is defined as *D* and its thickness is defined as *h*. To eliminate the influence of the *z*-axis direction, *h* was fixed at 2 mm for all printed structures. For comparison purposes, a control sample was also printed using the standard printing process, with each layer cured using 2-second light exposure on a LittleRP DLP printer.

The subdivision strategy was employed to print the disc structure. The layer was cured by using sequential images generated by the breadth-first search algorithm (BFS) [13]. The algorithm solidified each cross-section layer with a fixed number of pixels, starting from the center point and moving towards the periphery. By using BFS algorithm, each cross-section layer image started from the edge and moved towards the center, and the pixels were combined in reverse order to ensure that the central part was printed first. For the disc structure, the pixels next to the black region were first extracted from the image. The initial image for each layer was a smaller disc at the center, followed by sequential rings (Figure 4 and Supporting Information Appendix A). The sequential images were generated by extracting a fixed number of pixels from the next level of the neighbouring image to achieve a quantifiable segmentation of the cross-section image.

Appendix A presents the printing process used to build a 32 mm (*D*) disc using different projection modes. The normal printing process involved printing the reference sample (Entry 1) by projecting each layer all at once ($n = 1$, no segmentation). Entries 2 to 4 describe three alternative projection modes that employ the subdivision strategy, where cross-section images are divided into sequential segments based on the number of pixels in each

step image. For example, in Entry 2, the cross-section image of the 32 mm diameter disc was divided into 10 sequential images, each with a fixed pixel number (30) per image. More sequential images were generated by further decreasing the pixel number. Entry 3 and 4 show that 15 and 21 sequential images were generated, respectively, with changes in the pixel size of the sub-images from 20 to 10 pixels. Table 1 summarizes the printed sizes of the discs and their corresponding building parameters using the subdivision strategy.

Table 1 Dimension of the printed discs and printing parameter for different entries.

Entry	*D* (mm)	*h* (mm)	Pixel number	Number (*n*) of sequential images*
1	32	2	∞	1
2	32	2	30px	10
3	32	2	20px	15
4	32	2	10px	30
5	16	2	∞	1
6	16	2	30px	5
7	16	2	20px	8
8	16	2	10px	15

**segmental images number that generated by using the subdivision strategy for one cross-section image*

Discs with diameter of 32 and 16 mm were printed according to the conditions listed in Table 1. Printed discs were removed from the platform and post processed in a UV oven for 15 minutes. After drying, the discs were mounted onto a 3D scanner to collect 3D images, as shown in Table S1. The point cloud on the bottom surface was extracted and registered with the original model using the least-squares method. Then, it was translated in the *z*-direction to allow the center to pass the $z = 0$ plane. The surface height (z) in the *z*-axis was fitted with a polynomial function using the least-squares method, considering the first and second factors that represent asymmetry and curvature, respectively. Factors of higher levels and on the *x*-*y* plane were ignored as the shape is curved symmetrically. The resulting point cloud was fitted with a quadric function:

$$z = ax^2 + by^2 + cx + dy \qquad (7)$$

where *a* is the curvature along the *x*-direction, *b* is curvature along the *y*-direction, *c* is the asymmetry along the *x*-direction and *d* is the asymmetry on *y*-direction. These images were combined in Figure 5 and the calculated results were summarized in Table 2.

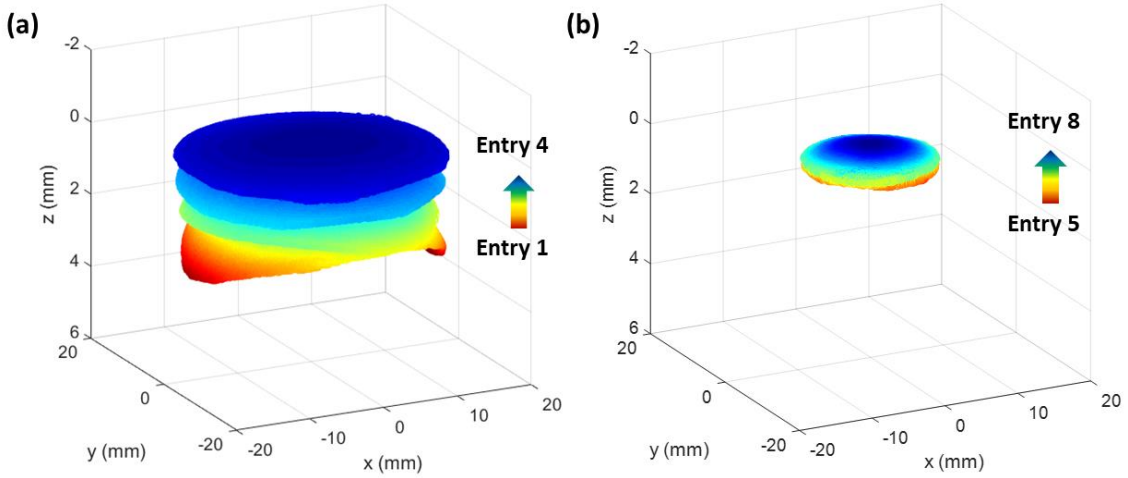

Figure 5 The combined scanning images of printed discs. (a) images of the discs with diameter of 32 mm (entry 1-4) and (b) images of discs with diameter of 16 mm (entry 5-8) that printed according to Table 1.

Table 2. Accuracy evaluation of the printed discs under conditions listed in Table 1.

Entry	a	b	c	d	Δz_{max}
1	0.011582922	0.00676809	2.90408E-05	1.69029E-06	2.96569E+00
2	0.007348418	0.006742572	5.31479E-05	5.42683E-07	1.88205E+00
3	0.004670822	0.004927692	1.46932E-05	1.43764E-05	1.26172E+00
4	0.001198079	0.001183823	5.78481E-07	4.86532E-06	3.06717E-01
5	0.013365611	0.012579942	2.38264E-05	8.3688E-06	8.55590E-01
6	0.007025979	0.007282193	3.03831E-05	2.86031E-05	4.66289E-01
7	0.004817568	0.005212842	1.49238E-05	2.14178E-05	3.33793E-01
8	0.003934663	0.00372384	7.4724E-06	6.08658E-06	2.51878E-01

Both Figure 5 and Table 2 demonstrate that the implementation of the subdivision strategy results in a significant improvement in dimension accuracy in 3D printing. The curvature in all directions is notably reduced compared to the reference sample, indicating that the subdivision strategy is an effective approach for enhancing printing accuracy. As

expected, an increase in the number of segments for each layer leads to further improved printing accuracy; the smaller pixel numbers for sequential images, the higher accuracy in the printed structures. For example, the curvature in the *x* and *y* directions decreased from 0.0073 and 0.0067 to 0.001198 and 0.001183, respectively, when the pixel number was reduced from 30 to 10. This suggests that theoretically, printing structures without distortion could be achieved with infinite segmentation of the layer image. Moreover, the successful printing rate is significantly improved with the implementation of the subdivision strategy. As previously noted, typical printing processes of the HDDA resins often result in failed prints due to the delamination of the structure from the platform during printing. However, no failure in the printing of the HDDA structure was observed when the subdivision strategy was implemented.

To assess the effectiveness of the subdivision strategy for different building sizes, we applied the approach to a smaller disc with a diameter of 16 mm. Table 1 outlines the printing parameters of the smaller disc, and the scanning results are summarized in Table 2 and Figure 5b. Interestingly, when comparing the evaluation results for discs with diameters of 32 and 16 mm, we observed that for larger building sizes, a greater improvement in accuracy under the same pixel number for sequential images was achieved. This phenomenon can be attributed to the negative correlation between the number of segments and building sizes when the cross-section image is divided by the same pixel number. Specifically, larger building sizes generated more segments, indicating that the number of segments, not pixels for the sequential image, is the determining factor in reducing curling stress and improving printing accuracy.

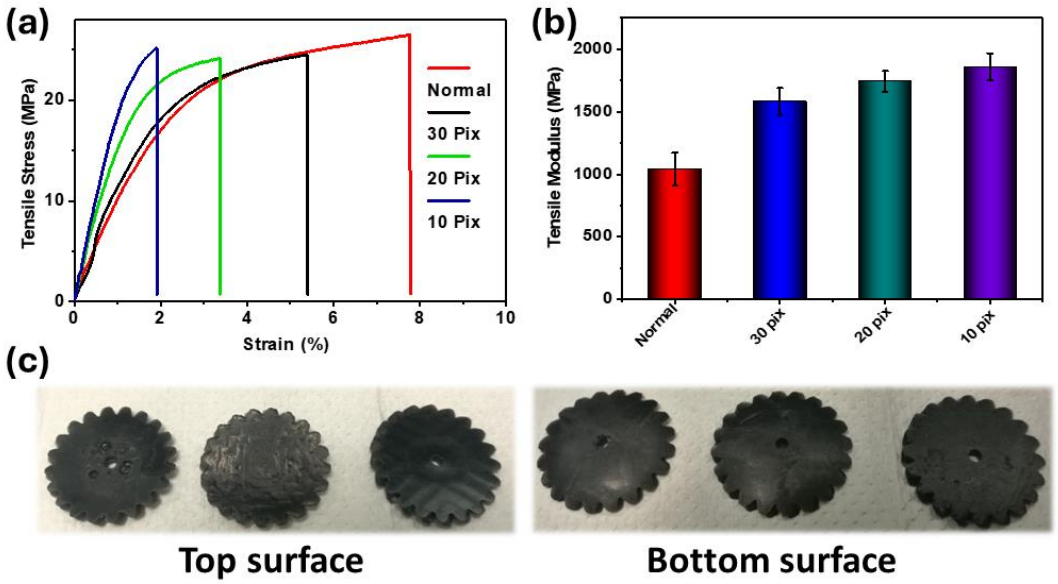

Figure 6 Mechanical properties of printed samples and the application of the subdivision strategy for gear printing. (a) Tensile stress-strain curves of printed specimens. (b) The comparison of the elastic modulus of the printed samples. (c) Top and bottom surface image of the printed gear with different conditions: left: normal condition; central: 50 pixels; right 10 pixels.

An additional benefit of using the subdivision strategy for 3D printing is that it can improve the mechanical performance of the printed structures. Figure 6a-b provide a comparison of the mechanical properties of specimens printed using the normal printing process (with a single layer image projection) versus those printed with the subdivision strategy using different curing modes. All specimens were fully cured through optimal printing conditions and post-treatment, with their mechanical properties aligning with the typical range reported for polyHDDA. The results clearly indicate a significant improvement in mechanical performance when the subdivision strategy is used. As shown in Figure 6b, printing with a resolution of 30 pixels using the subdivision strategy resulted in a 52% increase in the elastic modulus compared to the normal printing process. Moreover, as the pixel resolution increased from 30 to 10 pixels, the elastic modulus continued to increase, and a higher increase of 78.4% was observed when the samples were printed with a resolution of 10 pixels.

Achieving dimensional accuracy is crucial for gears to perform efficiently and quietly. To demonstrate the effectiveness of the subdivision strategy in improving printing accuracy, a gear structure was printed as shown in Figure 6c. For comparison, the gear structure was first printed using the normal DLP process (one-time exposure). As expected, serious curling and distortion were observed in the reference sample. In contrast, when employing the subdivision strategy, we observed significant decreases in distortion. We used 50 and 10 pixels division steps to investigate the effect of pixel number on printing accuracy (Supporting Information, Appendix B). Our results show that using more sequential images for printing (with fewer pixels defined for each sequential image) resulted in higher printing accuracy and less distortion. These findings highlight the effectiveness of the subdivision strategy in improving the printing accuracy of complex structures, such as gears, which require high dimensional accuracy.

2.4 Applying Subdivision Strategies in Practical DLP 3D Printing

Based on the above discussion, it is evident that the subdivision strategy helps reduce accumulated curl distortion and minimize heat generation during the printing process. To simplify this strategy for practical applications, we found that converting the solid structure to a grid structure can further improve printing accuracy, provided it does not affect the application or mechanical requirements.

Figure 7a illustrates the STL files of identical ring structures designed as both solid and grid structures, along with the corresponding 3D printed versions using resin. For easy comparison, three notches are designed inside the structures to facilitate image comparison and printing accuracy evaluation. In our demonstration, we modified one of our lab-developed resins (formula detailed in the supporting information) because neat HDDA led to severe curling and printing failure with Resin I. However, HDDA was still used in Resin II to

highlight its high curling effect. Significant deformation was observed when printing the solid structure, whereas the ring structure designed with hollow grids printed successfully.

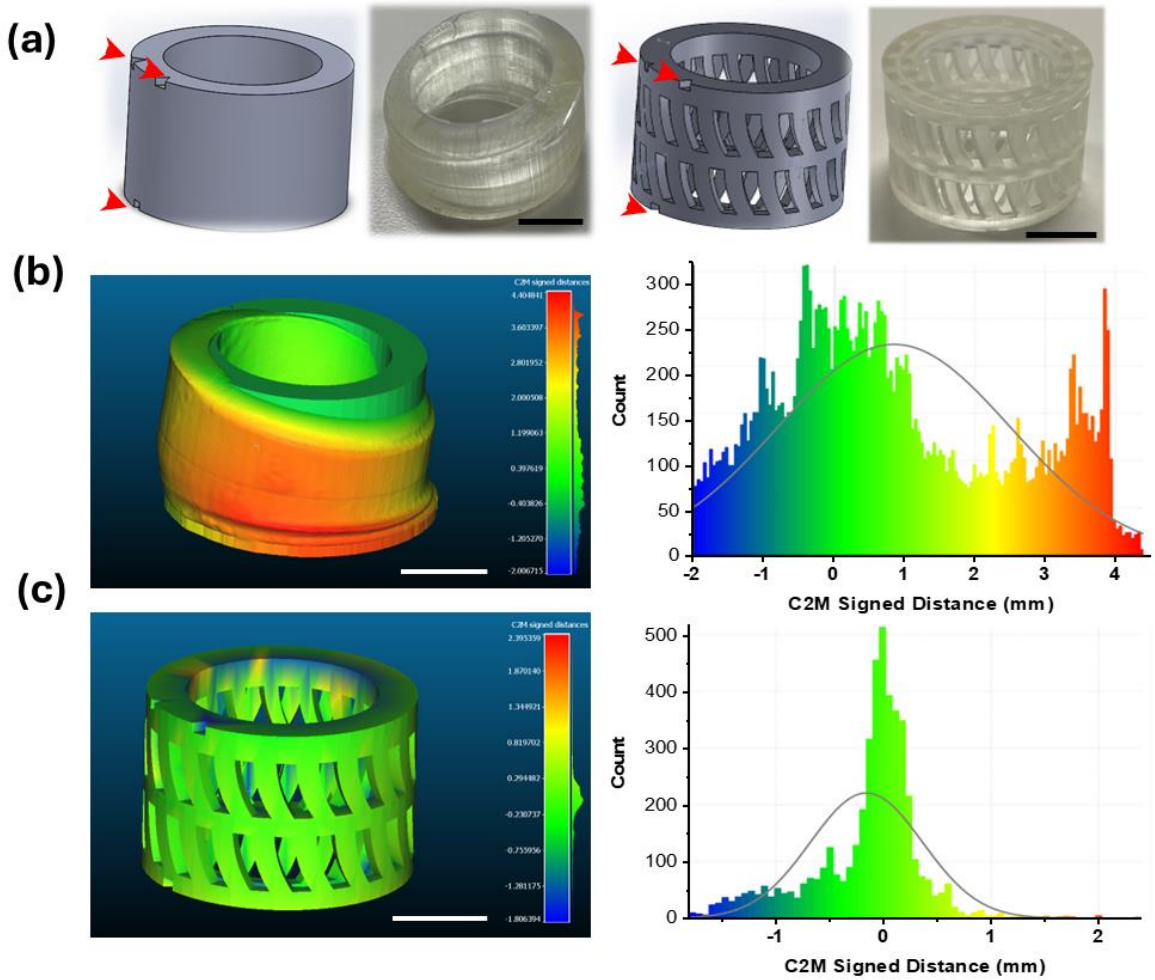

Figure 7 Printing accuracy evaluation. (a) The STL files and printed products of the ring that designed with solid and grid structure. (b and c) Dimensional accuracy measurement of using cloud compare software of the 3D printed ring with (b) solid structure and (b) grid structure. Scale bar: 10 mm.

To better understand the differences, the DLP-printed models were sprayed with white paint to reduce light refraction, enabling accurate surface scanning. The models were scanned using a 3Shape E4 scanner to obtain the STL files, which were then compared with the reference STL files using CloudCompare software. The designed triangular notches aided in aligning the original and scanned STL images. Figure 7b shows the comparison between the

original STL file of the solid ring and the scanned STL file of the printed ring, revealing a printing resolution within the range of 1.65 ± 0.84 mm. There was a significant discrepancy in the printing resolution of Resin II. However, when the ring structure was printed using the grid design, which mitigates curling and heat effects during 3D printing, the printed ring exhibited a resolution of 0.51 ± 0.15 mm, much better than the solid ring. This results suggests that the subdivision strategy can be effectively employed to improve printing accuracy in a simple and practical way by using a grid design rather than a solid structure, particularly when accuracy is paramount.

3. Conclusions

In summary, the present study introduces a strategy to reduce the persistent challenge of curling distortion and heat effect in VPP-based DLP printing technology. Our approach involves dividing the printing cross-section image into sub-images and curing in a ripple development manner, resulting in significant improvement in printing accuracy and mechanical performance. Our findings demonstrate that increasing the number of sub images can further enhance printing accuracy and mechanical performance, presenting a valuable avenue for future research. However, it should be noted that the rippling curing process can extend printing time, and additional research is necessary to fully comprehend its effects on the shrinkage and accuracy of 3D printing. Hence, we demonstrate that subdivision strategy can be achieved simply by design the solid structure into grid one in practical 3D printing, which helps to mitigate heat effect during polymer curing and reduce polymer distortion. These findings suggest that the subdivision strategy can effectively tackle the printing challenges associated with both resin volume shrinkage and heat-induced distortion, which have long been a persistent issue in DLP printing technology.

4. Materials and Methods

4.1 Materials and Equipment

1,6-Hexanediol diacrylate (80%), Phenylbis(2,4,6-trimethylbenzoyl)phosphine oxide (97%), chromium(VI) oxide, and Isopropanol were purchased from Merck and used directly. Carbon black (LOT-3301803) was purchased from Cabot. DLP 3D printer for the resin test was LittleRP using DLP projector (Brand & model: Acer P1283) as light source and Creation Workshop as printing control software. Printing was carried out with slice thickness of 0.05mm. The disc 3D structures were created in Sketchup and sliced with Creation Workshop.

4.2 Resin Preparation and Shrinkage Test

To prepare the printing ink, HDDA and pigment (carbon black or chromium oxide) were weighed into a glass bottle and mixed with the aid of ultrasonication for at least 10 minutes. Then, phenylbis(2,4,6-trimethylbenzoyl)phosphine oxide was added, and the mixture was vigorously stirred overnight in the absence of light. To determine the densities of the monomers and polymers, liquid HDDA and solid polyHDDA were measured using a gas displacement Pycnometry system from Micromertics. Specifically, 1 ml of the liquids was weighed to determine the densities of the monomers, while samples of known dimensions were weighed to determine the densities of the polymers. Three measurements were made for each monomer or polymer sample, and the standard deviations were less than 1%.

4.3 Printing Test and Images Scanning

All the structures were printed on a DLP printer (LittleRP), with the conditions are listed in the Results Section. The printed structures were detached from the platform and washed with IPA, then further cured in UV oven (λ = 405 nm, power: 100 W) for 15 min. To enhance light reflection for the black samples, the collected printed structures were first coated with one layer of ZnO particles. Images of printed structures were collected on a Shining Scanner.

4.4 Temperature Monitoring

The experiment was carried out in a laboratory environment. A long-wave infrared (LWIR) camera (brand & model: FLIR A655SC) coupled with a 25 ° field of view (FOV) infrared lens was used to acquire the data. The frame rate for recording was set to 50Hz. To capture the data, the camera was placed on a tripod and positioned over the top of the resin at a distance and angle of approximately 400 mm and 20°, respectively. To record and analyze the data, the camera was connected to a laptop installed with the ResearchIR software from FLIR. Figure S4 depicts a schematic of the experimental setup while Table S2 indicates the experiment and camera settings used.

A silicon disc was placed over the resin to weigh it down and ensure a thin and even distribution was achieved. The camera's emissivity setting was set to 0.5 due to the presence of the silicon disc. The emissivity of the silicon disc was determined with the aid of a blackbody (brand & model: FLIR Blackbody Accessory - 4228308). The other camera settings were referenced from the atmospheric conditions within the laboratory. Additional details of the data acquisition and analysis procedure can be found in the supporting information.

Acknowledgments

This work was financially supported by SERC Central Research Fund (TIMR211001bSERCRF) of Agency for Science, Technology and Research (A*STAR) of Singapore and RIE2025 Manufacturing, Trade and Connectivity (MTC) Programmatic Fund. Grant No: M24N3b0028.

Author contributions:

Conceptualization: WFK

Math Modelling: ZY

Methodology: ZY, SP, VKS, YTC, PJ

Writing—original draft: WFK, ZY

Writing—review & editing: WFK, ANCY

Declaration of competing interest

The authors declare that they have no known competing financial interests or personal relationships that could have appeared to influence the work reported in this paper.

Data and materials availability

All data needed to evaluate the conclusions in the paper are present in the paper and/or the Supplementary Materials.

References

[1] a)V. F. Scalfani, T. P. Vaid, *Journal of Chemical Education* **2014**, 91, 1174; b)M. D. Symes, P. J. Kitson, J. Yan, C. J. Richmond, G. J. Cooper, R. W. Bowman, T. Vilbrandt, L. Cronin, *Nature chemistry* **2012**, 4, 349; c)H. Misawa, S. Juodkazis, *3D laser microfabrication: principles and applications*, John Wiley & Sons, **2006**; d)A. Jandyal, I. Chaturvedi, I. Wazir, A. Raina, M. I. U. Haq, *Sustainable Operations and Computers* **2022**, 3, 33.

[2] a)P. Parandoush, C. Zhou, D. Lin, *Advanced Engineering Materials* **2019**, 21, 1800622; b)Y. Guo, J. Xu, C. Yan, Y. Chen, X. Zhang, X. Jia, Y. Liu, X. Wang, F. Zhou, *Advanced Engineering Materials* **2019**, 21, 1801314; c)M. Hegde, V. Meenakshisundaram, N. Chartrain, S. Sekhar, D. Tafti, C. B. Williams, T. E. Long, *Advanced Materials* **2017**, 29, 1701240; d)S. Ford, T. Minshall, **2019**; e)Y. Chen, Z. Zou, T. Fu, Z. Li, Z. Zhang, M. Zhu, Q. Gao, S. Wu, G. Fu, Y. He, *International Journal of Extreme Manufacturing* **2024**, 6, 035503; f)H. Wang, S. Liu, X. Yin, M. Huang, Y. Fu, X. Chen, C. Wang, J. Sun, X. Yan, J. Han, *International Journal of Extreme Manufacturing* **2024**, 6, 045004; g)M. Zhou, T. Yuan, L. Shang, *Research* **2024**, 7, 0446.

[3] a)J. K. Placone, A. J. Engler, *Advanced healthcare materials* **2018**, 7, 1701161; b)J. W. Stansbury, M. J. Idacavage, *Dental materials* **2016**, 32, 54; c)Y. J. Choi, T. G. Kim, J. Jeong, H. G. Yi, J. W. Park, W. Hwang, D. W. Cho, *Advanced healthcare materials* **2016**, 5, 2636; d)P. Robles Martinez, UCL (University College London), 2019; e)G. Chen, Y. Xu, P. C. L. Kwok, L. Kang, *Additive Manufacturing* **2020**, 34, 101209.

[4] a)E. Andrzejewska, *Progress in polymer science* **2001**, 26, 605; b)A. P. Keating, J. Knox, R. Bibb, A. I. Zhurov, *Journal of orthodontics* **2008**, 35, 191; c)H. Quan, T. Zhang, H. Xu, S. Luo, J. Nie, X. Zhu, *Bioactive materials* **2020**, 5, 110; d)A. Andreu, P.-C. Su, J.-H. Kim, C. S. Ng, S. Kim, I. Kim, J. Lee, J. Noh, A. S. Subramanian, Y.-J. Yoon, *Additive Manufacturing* **2021**, 44, 102024; e)X. Zhang, F. Liu, B. Du, R. Huang, S. Zhang, Y. He, H. Wang, J. Cui, B. Zhang, T. Yu, *Research* **2022**.

[5] a)X. Kuang, K. Chen, C. K. Dunn, J. Wu, V. C. Li, H. J. Qi, *ACS applied materials & interfaces* **2018**, 10, 7381; b)J. Fuh, L. Lu, C. Tan, Z. Shen, S. Chew, *Journal of Materials Processing Technology* **1999**, 89, 211.

[6] Z. Weng, X. Huang, S. Peng, L. Zheng, L. Wu, *Nature Communications* **2023**, 14, 4303.
[7] a)W. Wang, C. Cheah, J. Fuh, L. Lu, *Materials & Design* **1996**, 17, 205; b)D. Karalekas, A. Aggelopoulos, *Journal of materials processing technology* **2003**, 136, 146; c)T. Mukherjee, V. Manvatkar, A. De, T. DebRoy, *Scripta materialia* **2017**, 127, 79; d)M. Kaveh, M. Badrossamay, E. Foroozmehr, A. H. Etefagh, *Journal of materials processing technology* **2015**, 226, 280.
[8] a)J. Han, S. Jiang, Y. Gao, F. Sun, *Journal of Materials Chemistry C* **2016**, 4, 10675; b)R. R. Moraes, J. W. Garcia, M. D. Barros, S. H. Lewis, C. S. Pfeifer, J. Liu, J. W. Stansbury, *Dental Materials* **2011**, 27, 509; c)S. Schoerpf, Y. Catel, N. Moszner, C. Gorsche, R. Liska, *Polymer Chemistry* **2019**, 10, 1357; d)R. Hoogenboom, *Angewandte Chemie International Edition* **2010**, 49, 3415; e)H. L. Chee, J. W. Koo, E. E. I. Sim, Q. Zhu, X. Gao, M. F. H. Ramli, J. L. Young, A. W. Holle, F. Wang, *Advanced Materials Technologies*, 2302230; f)Y. Han, C. C. J. Yeo, D. Chen, F. Wang, Y. Chong, X. Li, X. Jiao, F. Wang, *New Journal of Chemistry* **2017**, 41, 8407.
[9] a)K. Tong, S. Joshi, E. A. Lehtihet, *Rapid Prototyping Journal* **2008**, 14, 4; b)K. Tong, E. Amine Lehtihet, S. Joshi, *Rapid Prototyping Journal* **2003**, 9, 301.
[10] a)E. Guven, Y. Karpat, M. Cakmakci, *Additive Manufacturing* **2022**, 57, 102954; b)S. M. Montgomery, F. Demoly, K. Zhou, H. J. Qi, *Advanced functional materials* **2023**, 33, 2213252.
[11] R. R. Braga, R. Y. Ballester, J. L. Ferracane, *Dental materials* **2005**, 21, 962.
[12] F. Wang, Y. Chong, F. Wang, C. He, *Journal of Applied Polymer Science* **2017**, 134, 44988.
[13] D. Rypl, Z. Bittnar, *Journal of Computational and Applied Mathematics* **2006**, 192, 148.
[14] a)B. Steyrer, B. Busetti, G. Harakály, R. Liska, J. Stampfl, *Additive Manufacturing* **2018**, 21, 209; b)Y. Suzuki, Y. Shinagawa, E. Kato, R. Mishima, K. Fukao, A. Matsumoto, *Macromolecules* **2021**, 54, 3293.